

Supporting Information

Toroidal moment and dynamical control in luminescent 1D and 3D terbium calixarene compounds

Hao Wang,^{ab#} Zhenhua Zhu,^{ac#} Léo La Droitte,^d Wuping Liao,^{*abe} Olivier Cador,^d Boris Le Guennic,^{*d} and Jinkui Tang^{*ab}

^a State Key Laboratory of Rare Earth Resource Utilization, Changchun Institute of Applied Chemistry, Chinese Academy of Sciences, Changchun 130022, China

^b School of Applied Chemistry and Engineering, University of Science and Technology of China, Hefei 230022, China

^c University of Chinese Academy of Sciences, Beijing 100049, China

^d Univ Rennes, CNRS, ISCR (Institut des Sciences Chimiques de Rennes) - UMR 6226, Rennes F-35000, France

^e Ganjiang Innovation Academy, Chinese Academy of Sciences, Ganzhou 341000, China

Equal contributions

* Corresponding authors

Contents

1. Synthesis and characterization	S2-S2
2. Crystallographic analysis and magnetic properties	S3-S8
3. Computational details	S9-S17
4. GC analysis and luminescent properties	S18-S20
5. References	S21-S22

1. Synthesis and characterization

Materials and measurements. *p*-*tert*-Butylthiacalix[4]arene (H₄TC4A) was synthesized by the literature method¹ and other reagents were purchased and used as received without any purification. Magnetic susceptibility measurement was performed on a Quantum Design MPMS XL-7 SQUID system under a 1000 Oe applied field at the temperature range of 2-300 K. Magnetic hysteresis was measured at 1.9 K under an average sweep rate of 31 Oe/s. The field dependence of magnetization was measured at 1.9 K, 3 K and 5 K. The TG-DSC was tested on a NETZSCH STA449F3 from room temperature to 900 °C under air atmosphere at a ramp rate of 10 °C/min. CHNS elemental analysis was recorded on a VarioEL instrument. Absolute Quantum yields were measured by C9920-2. Photoluminescence (PL) spectra were recorded with the excitation and emission bandpass of 1 nm and the time decay curves were acquired by an Edinburgh PLSP 920 spectrometer equipped with a Xe900 Lamp and a photomultiplier tube (R928P) at room temperature. The decay curves were fitted by a double exponential function of $y = \alpha_1 \exp(-t/\tau_1) + \alpha_2 \exp(-t/\tau_2) + y_0$. The average lifetimes were calculated according

$$\frac{\alpha_1 \tau_1^2 + \alpha_2 \tau_2^2}{\alpha_1 \tau_1 + \alpha_2 \tau_2}$$

to the following equation²: $\tau = \frac{\alpha_1 \tau_1^2 + \alpha_2 \tau_2^2}{\alpha_1 \tau_1 + \alpha_2 \tau_2}$

Syntheses of **1**, **1-180**, **1-180-CH₃OH** and **1-180-H₂O**.

Colorless flake crystals of **1** were obtained from the solvothermal reaction of the mixture of H₄TC4A (0.036 g, 0.05 mmol), Tb(Ac)₃·xH₂O (0.034 g, 0.1 mmol), benzophenone-4,4'-dicarboxylic acid (H₂bzpdcc) (0.027 g, 0.1 mmol), N, N-dimethylformamide (DMF, 2.5 mL), methanol (CH₃OH, 1 mL) in a 15 mL Teflon-lined autoclave which was kept at 130 °C for 3 days and then slowly cooled to 20 °C at 4 °C·h⁻¹. The crystals were isolated by filtration, which were washed using CH₃OH and then dried in air. Yield: ca. 70% based on H₄TC4A. Elemental analysis (%) for (H-DMF)⁺{Tb₄(TC4A)₂L₂(CH₃OH)₂(DMF)₂(μ₄-OH)}·13CH₃OH (C₁₃₄H₁₈₆N₃O₃₇S₈Tb₄): calculated C, 48.39; H, 5.60; N, 1.26; S, 7.70; Found: C, 48.23; H, 4.84; N, 0.97; S, 7.96.

1-180 were obtained by heating **1** at 180 °C under vacuum for 12 h.

1-180-CH₃OH were obtained by immersing sample **1-180** in CH₃OH for 10 h and then drying at air atmosphere.

1-180-H₂O were obtained by immersing sample **1-180** in distilled water for 5 h and then drying them at air atmosphere.

Synthesis of **2**.

Colorless strip crystals of **2** were obtained from the solvothermal reaction of the mixture of H₄TC4A (0.036 g, 0.025 mmol), Tb(Ac)₃·xH₂O (0.017 g, 0.05 mmol), H₂bzpdcc (0.014 g, 0.05 mmol), methanol (MeOH, 4 mL) in a 15 mL Teflon-lined autoclave which was kept at 130 °C for 3 days and then slowly cooled to 20 °C at 4 °C·h⁻¹. The crystals were isolated by filtration, which were washed using MeOH and then dried in air. Yield: ca. 25% based on H₄TC4A. CHS element analysis (%): for {Tb₄(TC4A)(HTC4A)L₂(CH₃OH)₄(μ₄-OH)}·5CH₃OH·6H₂O or C₁₁₉H₁₅₃O₃₄S₈Tb₄: calculated C, 47.31; H, 5.07; S, 8.48; Found: C, 47.12; H, 4.64; S, 8.87.

2. Crystallographic analysis and magnetic properties

Single-crystal structure determination.

The intensity data of **1** and **2** were recorded on a Bruker APEX-II system with Cu-K α radiation ($\lambda = 1.54178 \text{ \AA}$). The structures were solved in Olex2 with SHELXT using intrinsic phasing and were refined with SHELXL using least-squares minimization.³⁻⁵ All non-hydrogen atoms were refined anisotropically. All hydrogen atom positions were calculated geometrically and refined using the riding model. The selected crystallographic parameters and refinement details were listed in Tables S1-S2. The crystallographic information files (CIFs) including the HKL and RES data, and the IUCr CheckCIF reports (PDF formats) can be found in the supplemental materials. CCDC 2226312-2226313 contain the supplementary crystallographic data for this paper. These data can be obtained free of charge from The Cambridge Crystallographic Data Centre via www.ccdc.cam.ac.uk/data_request/cif.

Table S1. Crystal data and structure refinement for **1** and **2**

	CIAC-267 (1)	CIAC-268 (2)
Formula	C ₁₂₁ H ₁₃₃ N ₃ O ₂₄ S ₈ Tb ₄	C ₁₁₅ H ₁₂₄ O ₂₄ S ₈ Tb ₄
Formula Weight	2905.46	2782.29
<i>T</i> (K)	179(2)	180(2)
Crystal System	Triclinic	Monoclinic
Space Group (no.)	<i>P</i> -1	<i>C</i> 2/ <i>c</i>
<i>a</i> (Å)	19.1485(7)	12.7641(4)
<i>b</i> (Å)	19.6598(6)	57.5684(16)
<i>c</i> (Å)	21.4502(7)	36.0789(11)
α (°)	90.609(2)	90
β (°)	111.829(2)	94.785(10)
γ (°)	90.189(2)	90
<i>V</i> (Å ³)	7495.4(4)	26418.7(14)
<i>Z</i>	2	8
<i>D_c</i> (g cm ⁻³)	1.287	1.399
μ (mm ⁻¹)	10.602	12.000
<i>F</i> (000)	2920	11152
Total Data	145719	58631
Unique Data	18629	16159
<i>R</i> _{int}	0.0690	0.0357
GOF	1.056	1.057
<i>R</i> ₁ ^a [<i>I</i> > 2 σ (<i>I</i>)]	0.0577	0.0462
<i>wR</i> ₂ ^b (all data)	0.1552	0.1254

$$^a R_1 = \sum ||F_o| - |F_c|| / \sum |F_o|; ^b wR_2 = \{ \sum [w(F_o^2 - F_c^2)_2] / \sum [w(F_o^2)] \}^{1/2}$$

Table S2. Selected bond lengths (Å) for **1** and **2**

1			
Tb(1)-S(008)	2.922(2)	Tb(3)-S(007)#2	2.928(2)
Tb(1)-S(00A)#1	2.933(2)	Tb(3)-S(00B)	2.927(2)
Tb(1)-O(4)	2.412(6)	Tb(3)-O(9)#2	2.404(6)
Tb(1)-O(2)#1	2.384(6)	Tb(3)-O(13)	2.383(5)
Tb(1)-O(5)	2.370(6)	Tb(3)-O(20)#3	2.338(6)
Tb(1)-O(1)#1	2.422(6)	Tb(3)-O(12)	2.422(6)
Tb(1)-O(23)#4	2.343(6)	Tb(3)-O(11)#2	2.380(6)
Tb(1)-O(3)	2.6360(5)	Tb(3)-O(10)	2.6533(5)
Tb(1)-O(6)	2.275(6)	Tb(3)-O(16)	2.289(7)
Tb(2)-Tb(1)	3.6020(7)	Tb(4)-Tb(3)	3.6277(7)
Tb(2)-Tb(1)#1	3.6152(7)	Tb(4)-Tb(3)#2	3.6096(8)
Tb(2)-S(005)	2.947(2)	Tb(4)-S(006)	2.950(2)
Tb(2)-S(009)#1	2.957(2)	Tb(4)-S(00C)#2	2.952(2)
Tb(2)-O(4)#1	2.355(6)	Tb(4)-O(9)#2	2.375(6)
Tb(2)-O(2)#1	2.369(6)	Tb(4)-O(13)#2	2.368(6)
Tb(2)-O(5)	2.364(6)	Tb(4)-O(12)	2.362(6)
Tb(2)-O(1)	2.368(6)	Tb(4)-O(11)	2.364(6)
Tb(2)-O(7)	2.398(6)	Tb(4)-O(14)	2.374(6)
Tb(2)-O(8)	2.373(6)	Tb(4)-O(10)	2.4606(5)
Tb(2)-O(3)	2.4645(6)	Tb(4)-O(15)	2.397(6)

2			
Tb(1)-Tb(2)	3.6176(7)	Tb(3)-O(13)	2.362(5)
Tb(1)-Tb(2)#4	3.5900(6)	Tb(3)-O(17)	2.653(6)
Tb(1)-S(3)	2.9363(19)	Tb(3)-O(14)	2.321(6)
Tb(1)-S(1)#4	2.9544(18)	Tb(3)-O(14)#1	2.321(6)
Tb(1)-O(5)	2.364(5)	Tb(4)-Tb(3)	3.5965(6)
Tb(1)-O(4)	2.376(5)	Tb(4)-S(7)#1	2.8994(19)
Tb(1)-O(3)#4	2.387(5)	Tb(4)-S(5)	2.9101(19)
Tb(1)-O(6)	2.403(5)	Tb(4)-O(10)	2.357(4)
Tb(1)-O(1)#4	2.346(5)	Tb(4)-O(11)#1	2.365(4)
Tb(1)-O(2)	2.5515(4)	Tb(4)-O(12)	2.351(4)
Tb(1)-O(8)	2.335(5)	Tb(4)-O(13)#1	2.365(5)
Tb(2)-S(4)	2.897(2)	Tb(4)-O(17)	2.4265(5)
Tb(2)-S(2)#4	2.9161(19)	Tb(4)-O(15)	2.430(5)
Tb(2)-O(5)	2.358(5)	Tb(4)-O(16)	2.435(5)
Tb(2)-O(4)#4	2.368(5)	Tb(5)-Tb(4)#1	3.6046(6)
Tb(2)-O(3)#4	2.361(5)	Tb(5)-Tb(4)	3.6045(6)
Tb(2)-O(1)	2.397(5)	Tb(5)-S(6)	2.9353(17)
Tb(2)-O(7)	2.360(6)	Tb(5)-S(6)#1	2.9355(17)
Tb(2)-O(2)	2.5450(5)	Tb(5)-O(10)#1	2.373(4)
Tb(2)-O(9)	2.404(5)	Tb(5)-O(10)	2.374(4)
Tb(3)-S(8)	2.941(2)	Tb(5)-O(11)#1	2.370(4)
Tb(3)-S(8)#1	2.941(2)	Tb(5)-O(11)	2.370(4)
Tb(3)-O(12)	2.364(4)	Tb(5)-O(17)	2.667(6)

Tb(3)-O(12)#1	2.364(5)	Tb(5)-O(23)#2	2.340(5)
Tb(3)-O(13)#1	2.361(5)	Tb(5)-O(23)#3	2.340(5)

Table S3. Bond valence calculations for central O atom of Tb₄ unit in **1** and **2**.
O(3) in **1**

Atom	Atom	r (Distance)	r ₀	B	Bond Valence
O(3)	Tb(1)	2.6360(5)	2.049	0.37	0.2046
O(3)	Tb(1)	2.6360(5)	2.049	0.37	0.2046
O(3)	Tb(2)	2.4645(6)	2.049	0.37	0.3253
O(3)	Tb(2)	2.4645(6)	2.049	0.37	0.3253
					1.0598 (Sum)

O(10) in **1**

Atom	Atom	r (Distance)	r ₀	B	Bond Valence
O(10)	Tb(3)	2.6533(5)	2.049	0.37	0.1953
O(10)	Tb(3)	2.6533(5)	2.049	0.37	0.1953
O(10)	Tb(4)	2.4606(5)	2.049	0.37	0.3288
O(10)	Tb(4)	2.4606(5)	2.049	0.37	0.3288
					1.0482 (Sum)

O(2) in **2**

Atom	Atom	r (Distance)	r ₀	B	Bond Valence
O(2)	Tb(1)	2.5515(4)	2.049	0.37	0.2571
O(2)	Tb(1)	2.5515(4)	2.049	0.37	0.2571
O(2)	Tb(2)	2.5450(5)	2.049	0.37	0.2617
O(2)	Tb(2)	2.5450(5)	2.049	0.37	0.2617
					1.0376 (Sum)

O(17) in **2**

Atom	Atom	r (Distance)	r ₀	B	Bond Valence
O(17)	Tb(3)	2.653(6)	2.049	0.37	0.1955
O(17)	Tb(4)	2.4265(5)	2.049	0.37	0.3605
O(17)	Tb(4)	2.4265(5)	2.049	0.37	0.3605
O(17)	Tb(5)	2.667(6)	2.049	0.37	0.1882
					1.1047 (Sum)

The BVS results of ~1.8–2.0, ~1.0–1.2, and ~0.2–0.4 indicate non-, single-, and double-protonation of the O atom, respectively. The protonation level of central $\mu_4\text{-OH}^-$ ions was deduced by bond valence sum calculations.^{6,7}

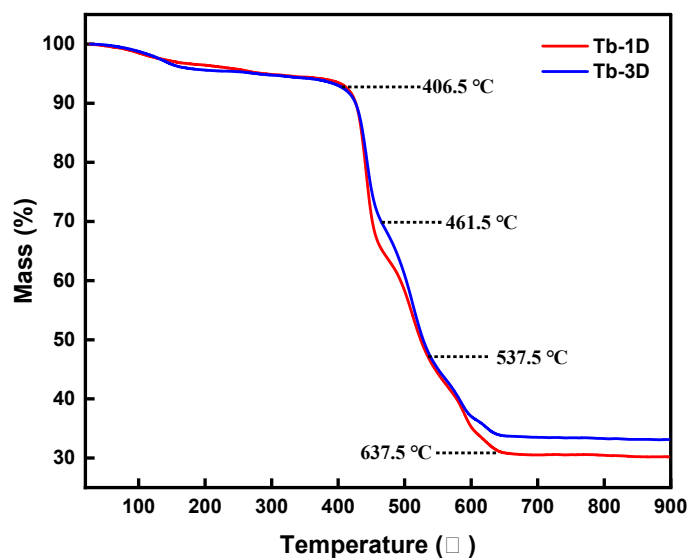


Fig. S1 TGA curves for **1** and **2** at a ramp rate of 10 °C/min in air.

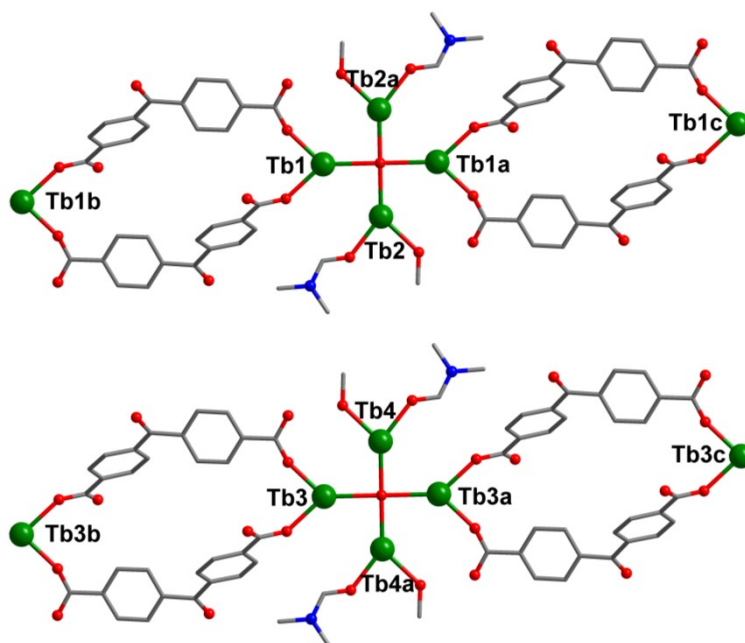


Fig. S2 Partial coordination environment of Tb(III) ions in Tb₄ unit from top view for **1** (green: Tb, red: O, grey: C, TC4A and all hydrogen atoms were omitted for clarity). Symmetry codes: upper: (a) 3-x, 2-y, 1-z; (b) 3-x, 1-y, 1-z; (c) x, 1+y, z. bottom: (a) 2-x, 1-y, 2-z; (b) 2-x, 2-y, 2-z; (c) x, -1+y, z.

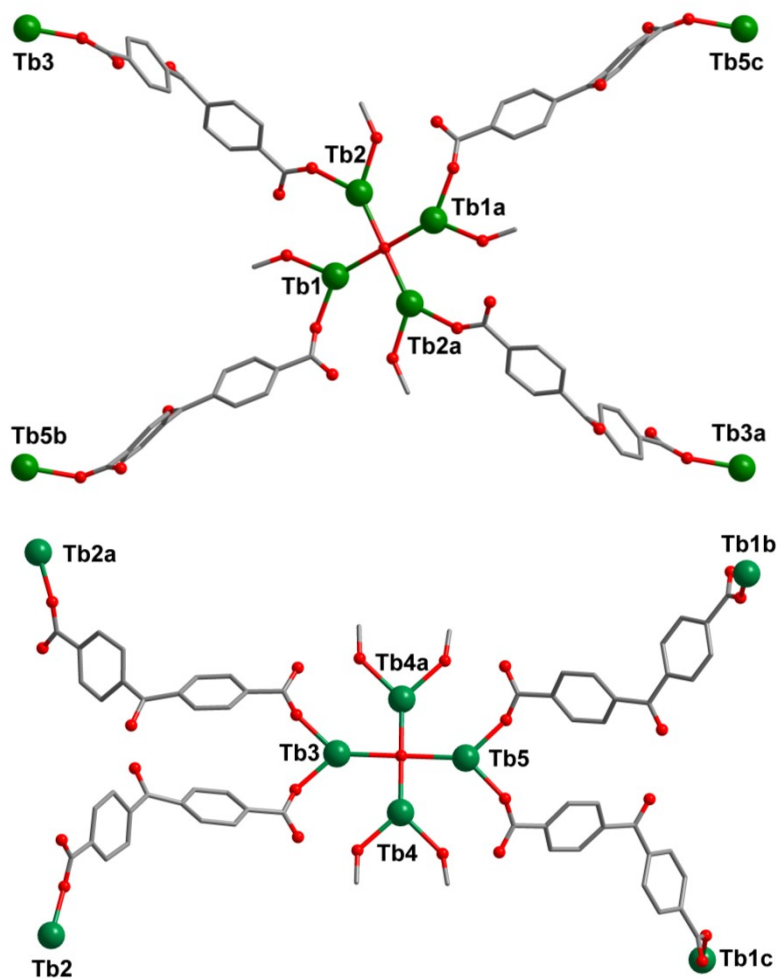


Fig. S3 Partial coordination environment of Tb(III) ions in unit1 (top) and unit2 (bottom) from top view for **2** (green: Tb, red: O, grey: C, TC4A and all hydrogen atoms were omitted for clarity). Symmetry codes: upper: (a) 0.5-x, 0.5-y, 1-z; (b) 2-x, 1-y, 1-z; (c) -1.5+x, -0.5+y, z. bottom: (a) 2-x, y, 1.5-z; (b) 2-x, 1-y, 1-z; (c) x, 1-y, 0.5+z.

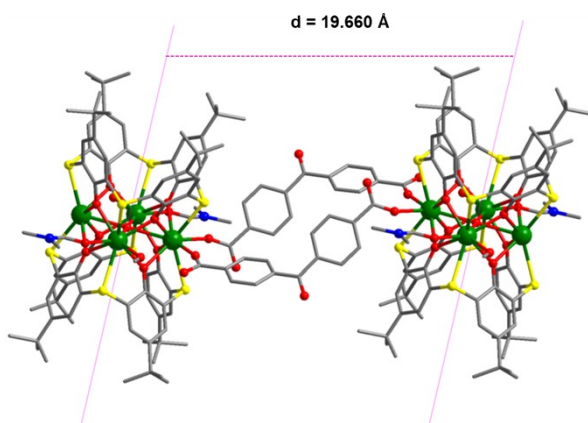


Fig. S4 The distance between two μ_4 -O atoms in adjacent Tb₄ units in **1**.

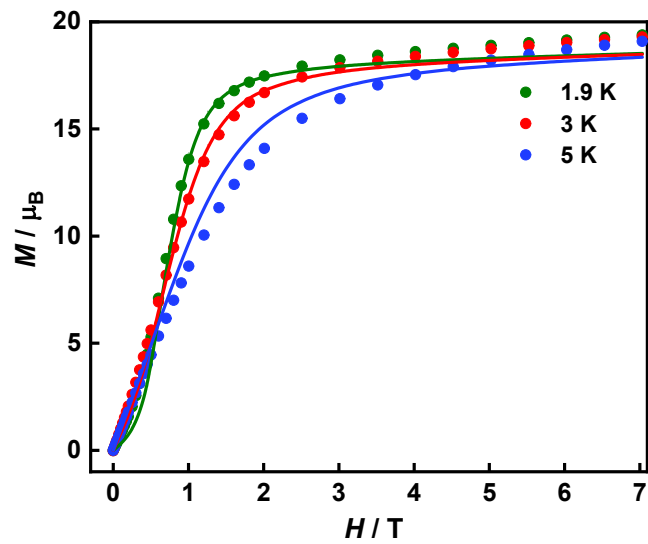


Fig. S5 Field dependences of magnetization in the field range 0-7 T at the range of 1.9 K - 5.0 K for **1**. Experimental values as solid cycles while the best calculated curves are represented as full lines.

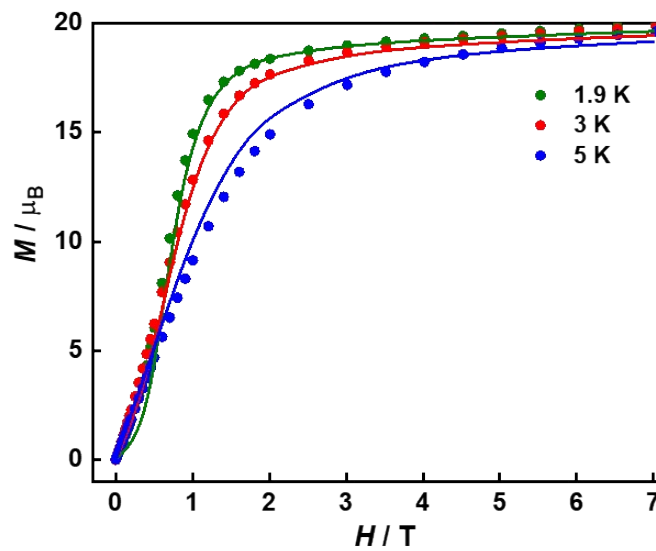


Fig. S6 Field dependences of magnetization in the field range 0-7 T at the range of 1.9 K - 5.0 K for **2**. Experimental values as empty cycles while the best calculated curves are represented as full lines.

3. Computational details

Atomic positions were extracted from the crystal structures obtained by X-ray diffraction. Due to the number of atoms in the complexes, a molecular model has been made out of the atomic positions obtained by X-ray diffraction for **Tb₄-3D** and **Tb₄-1D**, presented in Figure S11-2. The models are made out of the monomeric fragments of the complexes, from which the C(CH₃)₃ molecular fragments of the ligands are replaced by H atoms and the linking ligands are replaced by O₂CCH₃. Only the positions of the hydrogen atoms were optimized at the DFT level using the 2019 release of the Amsterdam Density Functional (ADF) package,⁸⁻¹⁰ while other atom positions were kept frozen. The calculations employed the revPBE functional,¹¹⁻¹² the triple- ζ polarized all-electron Slater type basis (TZP) from the ADF basis-set library, used the scalar relativistic (SR) all-electron zeroth-order regular approximation (ZORA) Hamiltonian¹³ and were performed in the unrestricted formalism by considering an open-shell octet spin state.

All wave function-based calculations were performed using the State-Averaged Complete Active Space Self-Consistent Field approach with Restricted-Active-Space-State-Interaction method (SA-CASSCF/RASSI-SO), as implemented in the *OpenMolcas* quantum-chemistry package (version 19.11).¹⁴ In this approach, the relativistic effects are treated in two steps on the basis of the Douglas–Kroll Hamiltonian.¹⁵ The scalar terms are included in the basis-set generation and are used to determine the CASSCF wave functions and energies.¹⁶ Spin-orbit coupling is then added within the RASSI-SO method, which mixes the calculated CASSCF spin free wave functions.¹⁷⁻¹⁸ Spin-orbit (SO) integrals are calculated using the AMFI (atomic mean-field integrals) approximation.¹⁹ The resulting spin-orbit wave functions and energies are used to compute the magnetic properties and g-tensors of the ground state and excited states multiplets following the pseudospin $S = 1/2$ formalism, as implemented in the SINGLE_ANISO routine.²⁰ Cholesky decomposition of the bielectronic integrals was employed to save disk space and to speed up the calculations.²¹ The active space consisted of the eight 4f electrons of the Tb^{III} ions spanning the seven 4f orbitals; CAS(8,7)SCF.

State-averaged CASSCF calculations were performed for all of the septets (7 roots), all of the quintets (140 roots), 91 out of the 588 triplets and 77 out of the 490 singlets of the Tb^{III} ion. In RASSI-SO, roots were mixed through spin-orbit coupling for the Tb^{III} ion, 7 septets, 140 quartets, 91 triplets and 77 singlets included. All atoms were described by ANO-RCC basis set. The following contractions were used: [8s7p5d3f2g1h] for the Tb, [7s6p4d2f1g] for the Y atoms, [4s3p1d] for the O, the N and the C atoms and [2s] for the H atoms.²²⁻²³

In both **1** and **2** tetranuclear complexes are centrosymmetric. Thus, calculations were performed on two non-equivalent Ln(III) center, with all the other Ln(III) centers replaced by the closed-shell Y(III) ion. Dipole-dipole magnetic couplings between the Ln(III) centers and magnetic properties of the complexes including the four Tb(III) centers were obtained using the POLY_ANISO routine.²⁴⁻²⁵ The intramolecular dipolar interactions are first calculated by the following equation:

$$E = \frac{\mu_0}{4\pi\vec{r}^3} \left[\vec{\mu}_1 \cdot \vec{\mu}_2 - \frac{3}{\vec{r}^2} (\vec{\mu}_1 \cdot \vec{r})(\vec{\mu}_2 \cdot \vec{r}) \right]$$

with \vec{r} the Tb–Tb vector, and $\vec{\mu}_1$ and $\vec{\mu}_2$ the magnetic moment vectors of the two Tb(III) centers. Then the exchange interaction in **1** and **2** can be fitted in relation to the experimental data by using the Lines model²⁶, where the following Hamiltonian is employed:

$$H = -J_{dip}(\mathfrak{S}_1\mathfrak{S}_2 + \mathfrak{S}_2\mathfrak{S}_3 + \mathfrak{S}_3\mathfrak{S}_4 + \mathfrak{S}_4\mathfrak{S}_1) - J_{exch}^{fit}(\mathfrak{S}_1\mathfrak{S}_2 + \mathfrak{S}_2\mathfrak{S}_3 + \mathfrak{S}_3\mathfrak{S}_4 + \mathfrak{S}_4\mathfrak{S}_1)$$

With \mathfrak{S} the pseudospin $\mathfrak{S} = 1/2$ operators at terbium sites. The best fitting value for J_{exch}^{fit} is selected by choosing the lowest standard deviation value between experimental and calculated magnetic susceptibility curves.

To give more insights into the orientation of the magnetic axis, the molecular electrostatic potential is calculated from the LOPROP charge analysis²⁷:

$$V(\vec{r}_i) = \sum_i^N \frac{q_i}{|\vec{r}_i - \vec{r}|} + \frac{\vec{p}_i \cdot \vec{r}_i}{|\vec{r}_i - \vec{r}|^3} + \frac{\vec{r}_i \cdot (\vec{Q}_i \times \vec{r}_i)}{|\vec{r}_i - \vec{r}|^5}$$

Where q_i , p_i , Q_i and r_i are respectively the charge, dipole, quadrupole moments, and displacement vector of the i -th atom. The resulting molecular electrostatic potential is mapped and represented in Fig. S14 and S15 using the home-made CAMMEL code (Calculated Molecular Multipolar Electrostatics). The potential is drawn on a sphere defined by the user around the central lanthanide ion, for a given state (the ground state in this case). For a clearer representation of the potential, the intensity can be directly related to both the color (red = high potential and blue = low potential) and the height of the irregularities. This program has already been used in previous works to give some hints on the orientation of magnetization axes.²⁸⁻³⁰ The CAMMEL code is available under GNU General Public License v3.0 and can be downloaded at <https://github.com/rmarchal1/CAMMEL>.

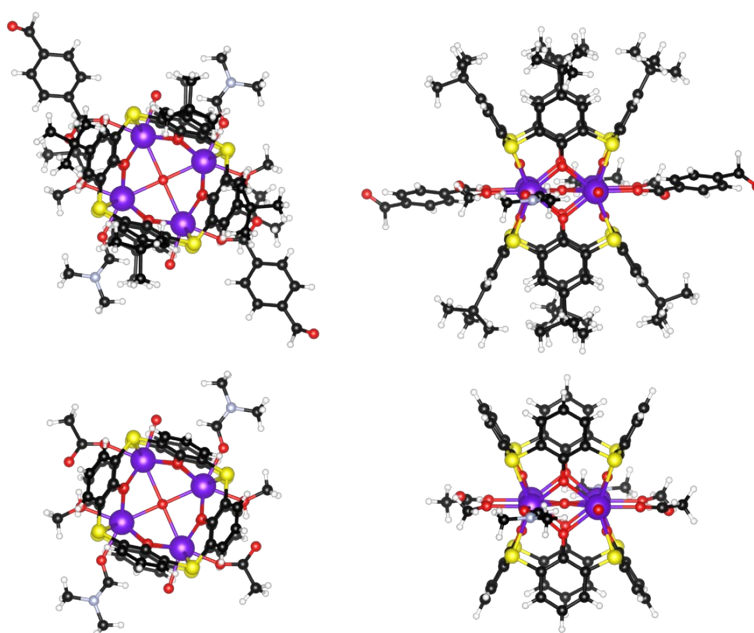


Fig. S7 Orthogonal views of monomeric fragment (top) and of molecular model (bottom) of **1**. Color codes: Tb, purple; S, yellow; O, red; N, light grey; C, black; H, white.

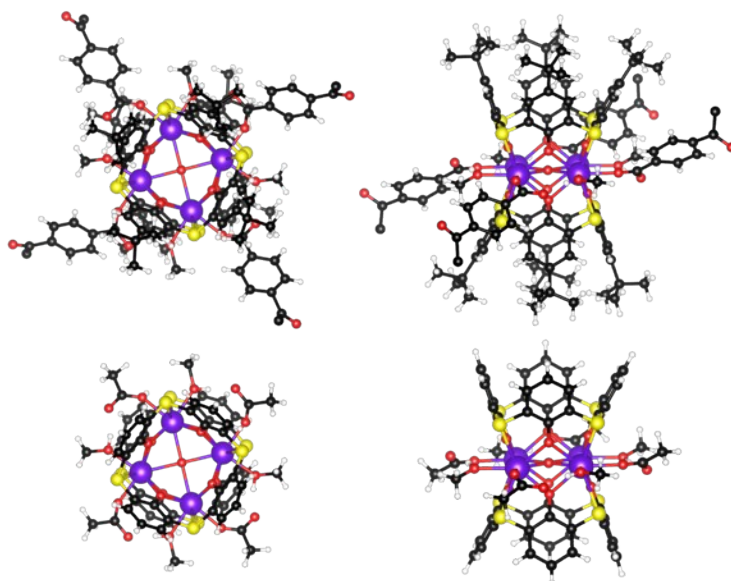


Fig. S8 Orthogonal views of monomeric fragment (top) and of molecular model (bottom) of **2**. Color codes: Tb, purple; S, yellow; O, red; C, black; H, white.

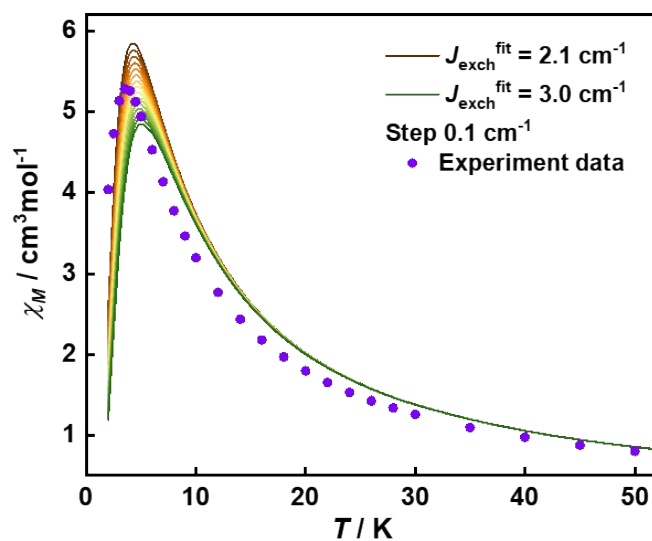


Fig. S9 Temperature dependent χ_M values for **1** in dots with the calculated curves in full lines for a screening of the $J_{\text{exch}}^{\text{fit}}$ value from 2 cm^{-1} to 3 cm^{-1} .

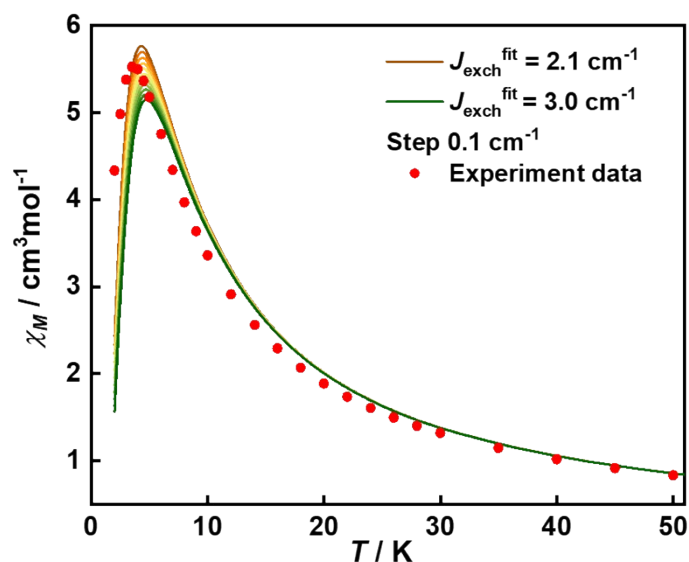


Fig. S10 Temperature dependent χ_M values for **2** in dots with the calculated curves in full lines for a screening of the $J_{\text{exch}}^{\text{fit}}$ value from 2 cm^{-1} to 3 cm^{-1} .

Table S4. Computed energy levels (the ground state is set at zero), main components (>10%) of the wavefunction for each m_j state of the ground-state multiplet 7F_6 and composition of the g -tensor (g_x , g_y , g_z) of the ground state for the first individual Tb center of **1** at the CAS(8,7)SCF/RASSI-SO level.

M	Energy (cm^{-1})	Wavefunction	
1	0.0	99.4% $ \pm 6\rangle$	
2	0.0	99.4% $ \pm 6\rangle$	
3	175.8	94.5% $ \pm 5\rangle$	
4	177.7	95.8% $ \pm 5\rangle$	
5	275.7	48.0% $ \pm 4\rangle$ + 32.4% $ \pm 2\rangle$ + 17.7% $ \pm 0\rangle$	
6	288.7	78.9% $ \pm 4\rangle$ + 17.2% $ \pm 2\rangle$	
7	299.2	63.6% $ \pm 1\rangle$ + 29.4% $ \pm 3\rangle$	
8	356.5	50.1% $ \pm 4\rangle$ + 25.4% $ \pm 0\rangle$ + 20.3% $ \pm 2\rangle$	
9	369.1	80.8% $ \pm 3\rangle$ + 10.3% $ \pm 1\rangle$	
10	468.5	56.2% $ \pm 2\rangle$ + 24.9% $ \pm 1\rangle$ + 13.4% $ \pm 4\rangle$	
11	468.8	47.6% $ \pm 3\rangle$ + 21.1% $ \pm 1\rangle$ + 15.7% $ \pm 0\rangle$ + 12.5% $ \pm 2\rangle$	
12	528.8	65.7% $ \pm 1\rangle$ + 15.9% $ \pm 2\rangle$ + 13.9% $ \pm 3\rangle$	
13	529.1	40.1% $ \pm 2\rangle$ + 37.6% $ \pm 0\rangle$ + 11.8% $ \pm 3\rangle$	
	g_x	g_y	g_z
	0.0	0.0	17.9

Table S5. Computed energy levels (the ground state is set at zero), main components (>10%) of the wavefunction for each m_j state of the ground-state multiplet 7F_6 and composition of the g -tensor (g_x , g_y , g_z) of the ground state for second individual Tb center of **1** at the CAS(8,7)SCF/RASSI-SO level.

M	Energy (cm ⁻¹)	Wavefunction	
1	0.0	99.3% ±6>	
2	0.0	99.0% ±6>	
3	149.7	77.4% ±5> + 18.3% ±3>	
4	150.2	64.8% ±5> + 13.2% ±3>	
5	196.1	47.1% ±4> + 29.8% ±0> + 17.9% ±2>	
6	239.9	59.2% ±4> + 13.9% ±2> + 10.3% ±1>	
7	248.7	70.1% ±1> + 21.4% ±3>	
8	302.5	56.8% ±4> + 22.5% ±0>	
9	318.4	76.7% ±3> + 12.1% ±1>	
10	459.1	60.2% ±2> + 23.6% ±1>	
11	459.5	53.1% ±3> + 22.3% ±1> + 16.8% ±0>	
12	567.6	74.3% ±1> + 19.7% ±2>	
13	568.0	51.0% ±2> + 37.2% ±0>	
	g_x	g_y	g_z
	0.0	0.0	17.9

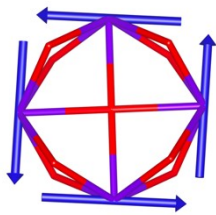
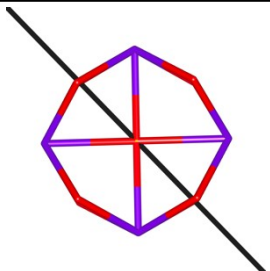
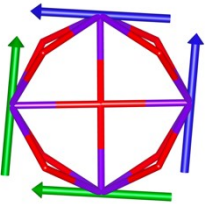
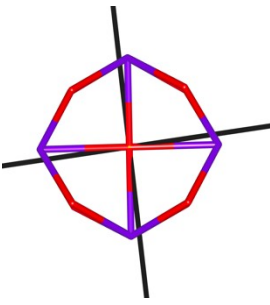
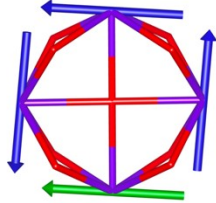
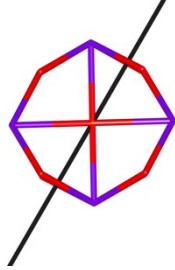
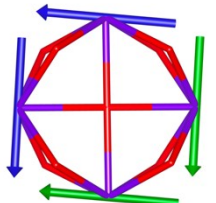
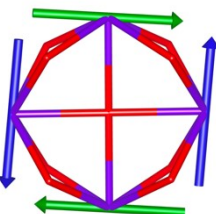
Table S6. Computed energy levels (the ground state is set at zero), main components (>10%) of the wavefunction for each m_j state of the ground-state multiplet 7F_6 and composition of the g -tensor (g_x , g_y , g_z) of the ground state for first individual Tb^{III} center of **2** at the CAS(8,7)SCF/RASSI-SO level.

M	Energy (cm ⁻¹)	Wavefunction
1	0.0	98.8% ±6>
2	0.0	98.8% ±6>
3	165.4	81.3% ±5> + 10.8% ±3>
4	168.1	87.7% ±5>
5	218.3	37.2% ±2> + 24.7% ±4> + 23.7% ±0> + 10.8% ±1>
6	244.9	54.1% ±1> + 16.4% ±5> + 16.1% ±3>
7	269.8	71.9% ±4> + 24.1% ±2>
8	359.8	69.6% ±4> + 19.6% ±0>
9	365.0	73.0% ±3> + 14.8% ±1> + 10.3% ±5>
10	517.5	73.2% ±2> + 24.8% ±4>
11	520.1	68.4% ±3> + 27.2% ±1>
12	629.2	82.0% ±1> + 16.6% ±3>
13	629.5	48.5% ±2> + 47.9% ±0>
	g_x	g_y
	0.0	0.0
		g_z
		17.8

Table S7. Computed energy levels (the ground state is set at zero), main components (>10%) of the wavefunction for each m_j state of the ground-state multiplet 7F_6 and composition of the g -tensor (g_x , g_y , g_z) of the ground state for second individual Tb center of **2** at the CAS(8,7)SCF/RASSI-SO level.

M	Energy (cm ⁻¹)	Wavefunction	
1	0.0	98.5% ±6>	
2	0.1	98.6% ±6>	
3	148.5	66.2% ±5> + 16.4% ±3> + 12.2% ±1>	
4	149.6	73.3% ±5> + 12.3% ±3>	
5	188.9	36.9% ±2> + 26.6% ±0> + 17.1% ±4> + 14.1% ±5>	
6	209.1	47.7% ±1> + 30.3% ±5> + 10.1% ±3>	
7	250.6	63.9% ±4> + 22.7% ±2> + 10.1% ±1>	
8	331.5	56.1% ±4> + 19.1% ±0> + 12.7% ±3>	
9	339.8	57.5% ±3> + 18.5% ±4> + 13.8% ±1>	
10	484.3	61.5% ±2> + 24.8% ±4>	
11	487.6	61.9% ±3> + 22.1% ±1> + 10.6% ±2>	
12	587.4	81.0% ±1> + 18.4% ±3>	
13	587.7	49.4% ±2> + 47.0% ±0>	
	g_x	g_y	g_z
	0.0	0.0	17.8

Table S8. Low-lying exchange states energies, global g values and orientations in pseudospin $\frac{1}{2}$, local g_z orientations and toroidal moment τ calculated in **2**.

E (cm ⁻¹)	Global g value	Global g orientation	Local g_z orientation	τ ($\mu_B \cdot \text{\AA}$)
0.00	0.0			10.15
0.00				
5.97	35.7			0.00
5.97				
6.03	5.5			5.07
6.05				
6.05				
6.05				
6.05				
6.05				
6.07				
6.13	35.9			0.00
6.13				
12.1	0.0			0.00
12.1				

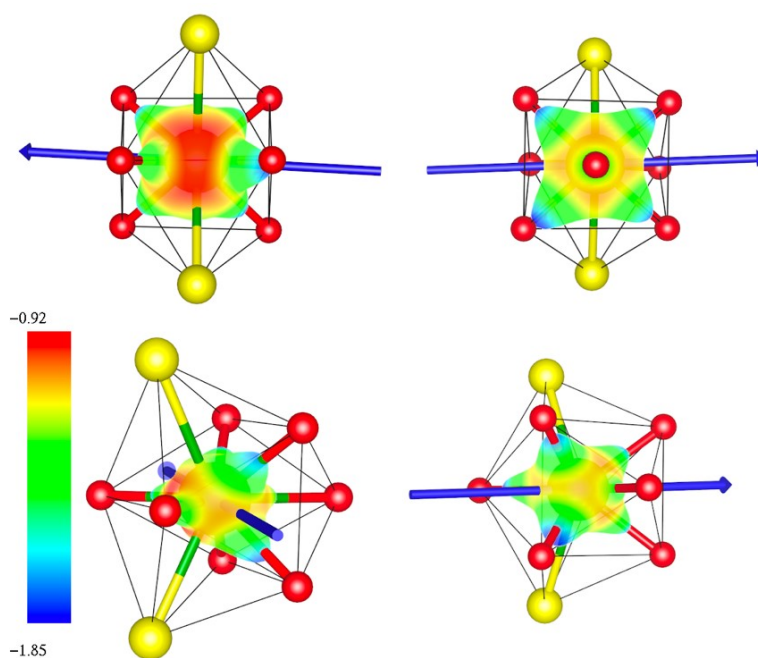


Fig. S11 Different views of the calculated total electrostatic potential (expressed in $e^- \text{ bohr}^{-1}$) at 3 Å around one Tb(III) ion, with the g_z direction in blue arrow for **1**. Color code: red = O; yellow = S; and green = Tb; H, C and N are omitted for clarity.

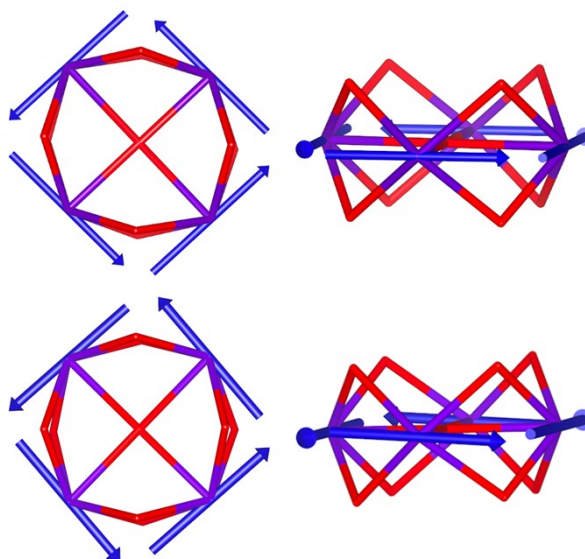


Fig. S12 “Top” view (left) and “side” view (right) of the computed ground-state anisotropy axes (blue) of **1** (top) and **2** (bottom) for the 2 non-equivalent Tb(III) centers. Color codes: Tb, purple; O, red, S, C and H are removed for clarity.

Table S9. Computed energy difference (ΔE) and exchange coupling constant (J_{exch}^{fit}) for **1** and **2**.

	J_{dip} (cm^{-1})	J_{exch}^{fit} (cm^{-1})
1	-4.31	2.6
2	-4.23	2.5

4. GC analysis and luminescent properties

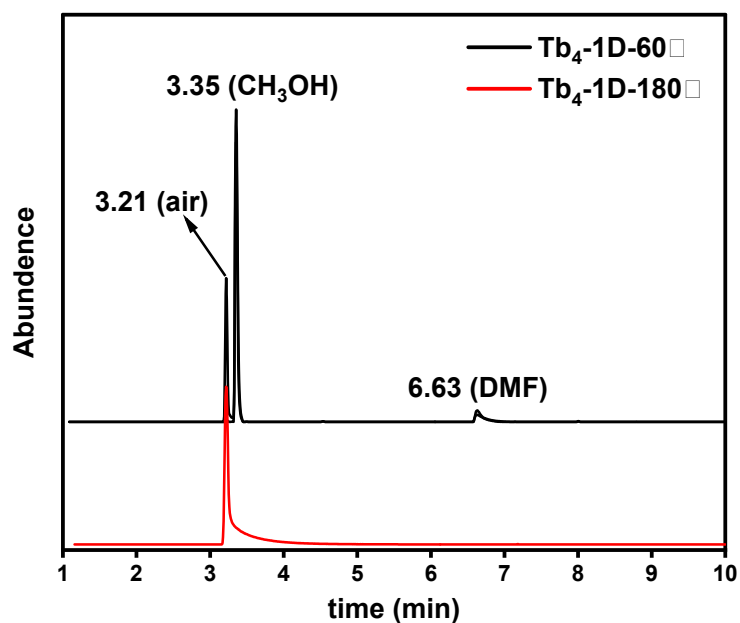


Fig. S13 GC-MS analysis of **1** at 60 °C and **1-180** at 180 °C.

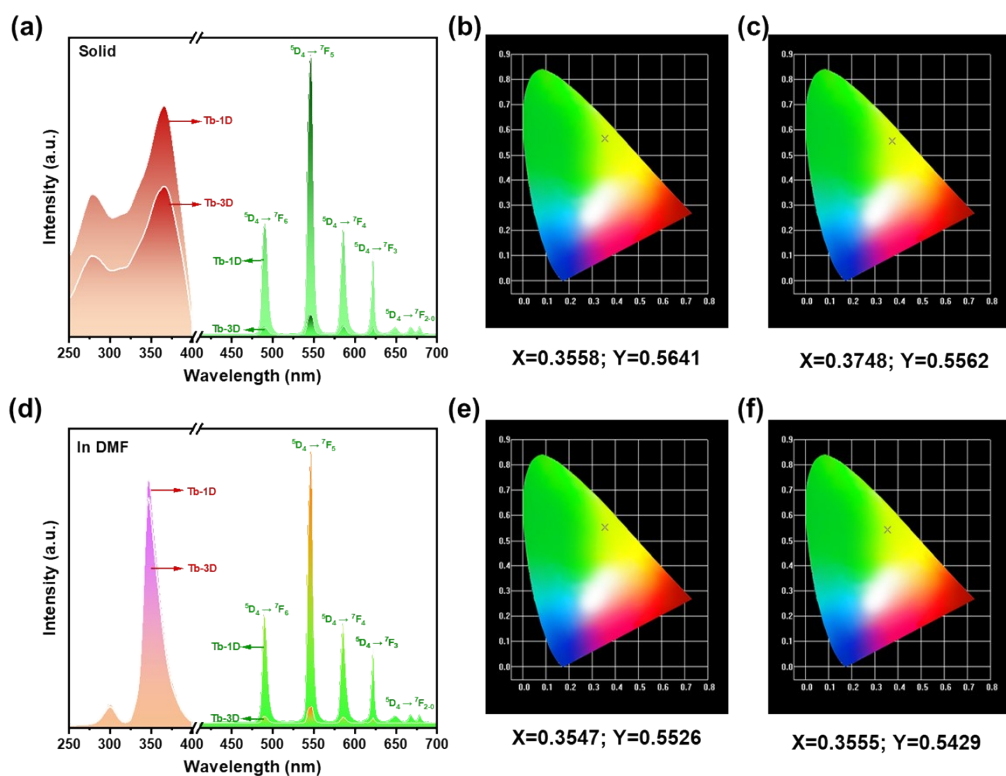


Fig. S14 Luminescence excitation and emission spectra at room temperature in solid (a) and DMF ($c = 2 \times 10^{-4}$ mol/L) (d) of **1** and **2**, as well as the CIE chromaticity diagrams in solid (**1**, b; **2**, c) and DMF solution (**1**, e; **2**, f) with $\lambda_{\text{ex}} = 365$ nm.

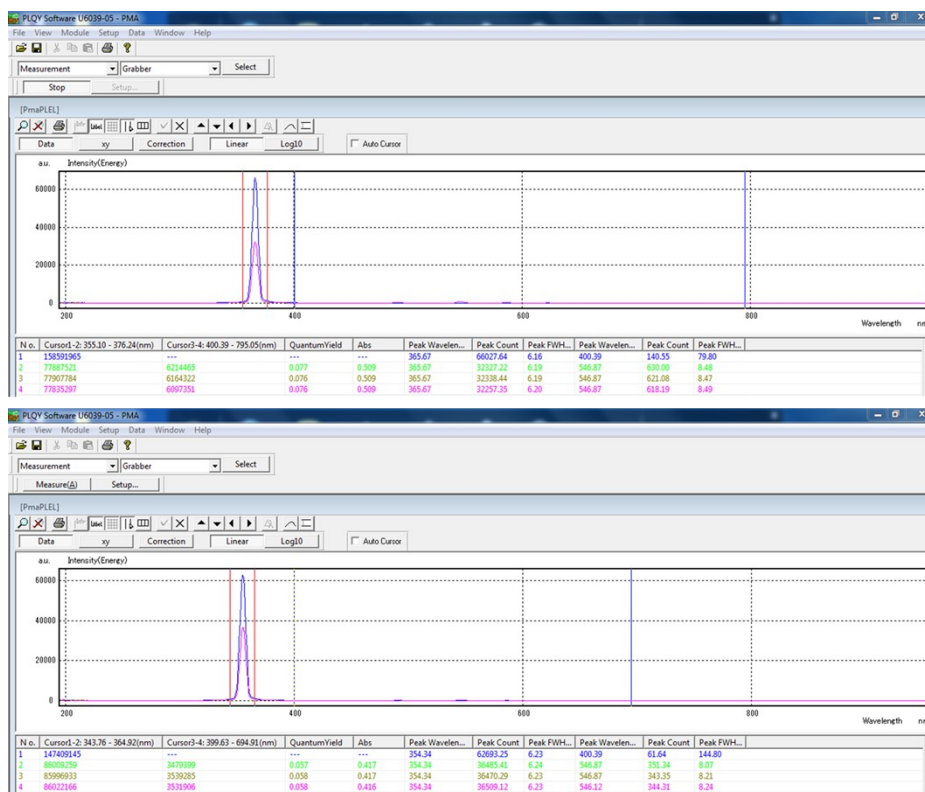


Fig. S15 The absolute QY measurements for **1** at room temperature in the solid state (top) and DMF solution (bottom).

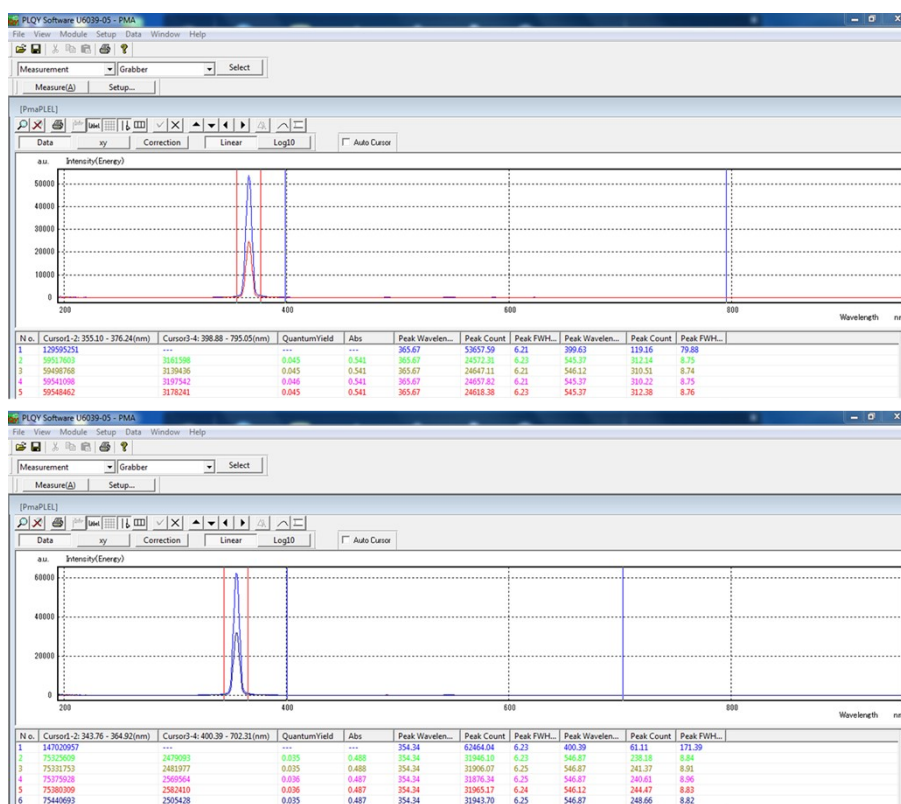


Fig. S16 The absolute QY measurements for **2** at room temperature in the solid state (top) and DMF solution (bottom).

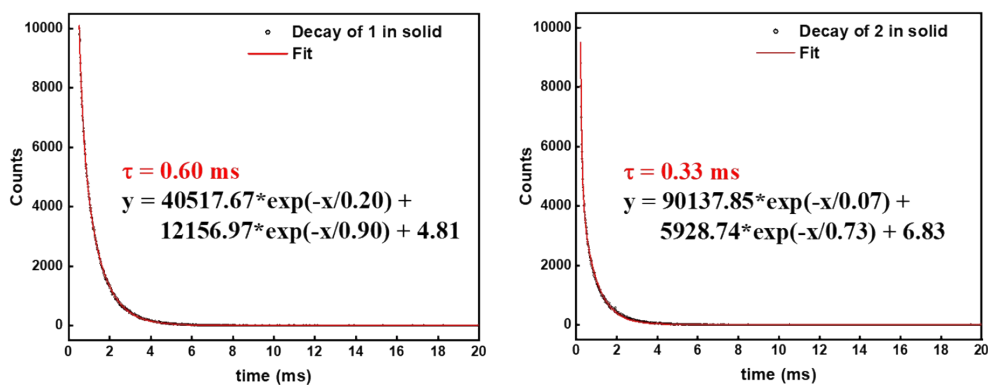


Fig. S17 Decay curves of **1** and **2** in the solid state at room temperature under $\lambda_{\text{ex}} = 365$ nm. Solid traces represent the fitting results.

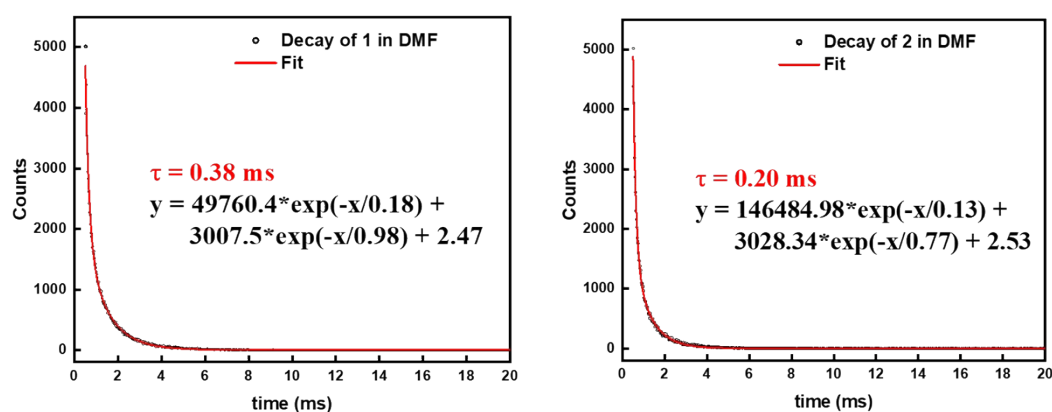


Fig. S18 Decay curves of **1** and **2** in DMF ($c = 2 \times 10^{-4}$ mol/L) at room temperature under $\lambda_{\text{ex}} = 365$ nm. Solid traces represent the fitting results.

5. References

1. Iki, N.; Kabuto, C.; Fukushima, T.; Kumagai, H.; Takeya, H.; Miyanari, S.; Miyashi, T.; Miyano, S., Synthesis of p-tert-butylthiacalix[4]arene and its inclusion property. *Tetrahedron* 2000, 56, 1437-1443.
2. Sillen, A.; Engelborghs, Y., The Correct Use of "Average" Fluorescence Parameters. *Photochem. Photobiol.* 1998, 67, 475-486.
3. Dolomanov, O. V.; Bourhis, L. J.; Gildea, R. J.; Howard, J. A. K.; Puschmann, H., OLEX2: a complete structure solution, refinement and analysis program. *J. Appl. Crystallogr.* 2009, 42, 339-341.
4. Sheldrick, G. M., Crystal structure refinement with SHELXL. *Acta Crystallogr. C Struct. Chem.* 2015, 71, 3-8.
5. Sheldrick, G. M., SHELXT - integrated space-group and crystal-structure determination. *Acta Crystallogr. A Found. Adv.* 2015, 71, 3-8.
6. Brese, N. E.; O'Keeffe, M., Bond-Valence Parameters for Solids. *Acta Cryst.* 1991, B47, 192-197.
7. Liu, W.; Thorp, H. H., Bond Valence Sum Analysis of Metal-Ligand Bond Lengths in Metalloenzymes and Model Complexes. 2. Refined Distances and Other Enzymes. *Inorg. Chem.* 1993, 32, 4102-4105.
8. te Velde, G.; Bickelhaupt, F. M.; Baerends, E. J.; Fonseca Guerra, C.; van Gisbergen, S. J. A.; Snijders, J. G.; Ziegler, T., Chemistry with ADF. *J. Comput. Chem.* 2001, 22, 931-967.
9. Guerra, C. F.; Snijders, J. G.; te Velde, G.; Baerends, E. J., Towards an order-N DFT method. *Theor. Chem. Acc.* 1998, 99, 391-403.
10. Amsterdam Density Functional (ADF), SCM Theoretical Chemistry; Vrije Universiteit: Amsterdam, The Netherlands, 2017. <http://www.scm.com>.
11. Perdew, J. P.; Burke, K.; Ernzerhof, M., Generalized Gradient Approximation Made Simple. *Phys. Rev. Lett.* 1996, 77, 3865-3868.
12. Ernzerhof, M.; Scuseria, G. E., Assessment of the Perdew–Burke–Ernzerhof exchange–correlation functional. *J. Chem. Phys.* 1999, 110, 5029-5036.
13. Lenthe, E. V.; Baerends, E. J.; Snijders, J. G., Relativistic regular two-component Hamiltonians. *J. Chem. Phys.* 1993, 99, 4597-4610.
14. Galván, I. F.; Vacher, M.; Alavi, A.; Angeli, C.; Aquilante, F.; Autschbach, J.; Bao, J. J.; Bokarev, S. I.; Bogdanov, N. A.; Carlson, R. K.; Chibotaru, L. F.; Creutzberg, J.; Dattani, N.; Delcey, M. G.; Dong, S. S.; Dreuw, A.; Freitag, L.; Frutos, L. M.; Gagliardi, L.; Gendron, F.; Giussani, A.; González, L.; Grell, G.; Guo, M.; Hoyer, C. E.; Johansson, M.; Keller, S.; Knecht, S.; Kovačević, G.; Källman, E.; Manni, G. L.; Lundberg, M.; Ma, Y.; Mai, S.; Malhado, J. P.; Malmqvist, P. Å.; Marquetand, P.; Mewes, S. A.; Norell, J.; Olivucci, M.; Oppel, M.; Phung, Q. M.; Pierloot, K.; Plasser, F.; Reiher, M.; Sand, A. M.; Schapiro, I.; Sharma, P.; Stein, C. J.; Sørensen, L. K.; Truhlar, D. G.; Ugandi, M.; Ungur, L.; Valentini, A.; Vancoillie, S.; Veryazov, V.; Weser, O.; Wesolowski, T. A.; Widmark, P.-O.; Wouters, S.; Zech, A.; Zobel, J. P.; Lindh, R., OpenMolcas: From Source Code to Insight. *J. Chem. Theory Comput* 2019, 15, 5925-5964.
15. Hess, B. A., Relativistic electronic-structure calculations employing a two-component no-pair formalism with external-field projection operators. *Phys. Rev. A* 1986, 33, 3742-3748.
16. Roos, B. O.; Taylor, P. R.; Sigbahn, P. E. M., A Complete Active Space SCF Method (CASSCF) Using a Density Matrix Formulated Super-CI Approach. *Chem. Phys.* 1980, 48, 157-173.

17. Malmqvist P. Å.; Roos B. O.; Schimmelpfennig B., The Restricted Active Space (RAS) State Interaction Approach with Spin-Orbit Coupling. *Chem. Phys. Lett.* 2002, 357, 230-240.
18. Malmqvist P.-Å.; Roos B. O., The CASSCF State Interaction Method. *Chem. Phys. Lett.* 1989, 155, 189-194.
19. Heß B. A.; Marian C. M.; Wahlgren U.; Gropen O., A meanfield spin-orbit method applicable to correlated wavefunctions. *Chem. Phys. Lett.* 1996, 251, 365-371.
20. Chibotaru, L. F.; Ungur, L., Ab Initio Calculation of Anisotropic Magnetic Properties of Complexes. I. Unique Definition of Pseudospin Hamiltonians and Their Derivation. *J. Chem. Phys.* 2012, 137, 064112.
21. Aquilante, F.; Malmqvist, P.-Å.; Pedersen, T.B.; Ghosh, A.; Roos, B.O., Cholesky Decomposition-Based Multiconfiguration Second-Order Perturbation Theory (CD-CASPT2): Application to the Spin-State Energetics of Co(III)(diiminato)(NPh). *J. Chem. Theory Comput.* 2008, 4, 694-702.
22. Roos, B. O.; Lindh, R.; Malmqvist, P.-Å.; Veryazov, V.; Widmark, P.-O., Main Group Atoms and Dimers Studied with A New Relativistic ANO Basis Set. *J. Phys.Chem. A.* 2004, 108, 2851-2858.
23. Roos, B. O.; Lindh, R.; Malmqvist, P.-Å.; Veryazov, V.; Widmark, P.-O.; Borin, A. C., New Relativistic Atomic Natural Orbital Basis Sets for Lanthanide Atoms with Applications to the Ce Diatom and LuF₃. *J. Phys. Chem. A.* 2008, 112, 11431-11435.
24. Chibotaru, L. F.; Ungur, L.; Soncini, A., The Origin of Nonmagnetic Kramers Doublets in the Ground State of Dysprosium Triangles: Evidence for a Toroidal Magnetic Moment. *Angew. Chem. Int. Ed.* 2008, 47, 4126-4129.
25. Ungur, L.; Van den Heuvel, W.; Chibotaru, L. F., Ab initio investigation of the non-collinear magnetic structure and the lowest magnetic excitations in dysprosium triangles. *New J. Chem.* 2009, 33, 1224-1230.
26. Lines, M. E., Orbital Angular Momentum in the Theory of Paramagnetic Clusters. *J. Chem. Phys.* 1971, 55, 2977-2984.
27. Gagliardi, L.; Lindh, R.; Karlström, G. Local properties of quantum chemical systems: The LoProp approach. *J. Chem. Phys.* 2004, 121, 4494-4500.
28. Zhang, K.; Montigaud, V.; Cador, O.; Li, G.-P.; Le Guennic, B.; Tang, J.; Wang, Y.-Y., Tuning the Magnetic Interactions in Dy(III)₄ Single-Molecule Magnets. *Inorg. Chem.* 2018, 57, 8550-8557.
29. Huang, G.; Fernandez-Garcia, G.; Badiane, I.; Camarra, M.; Freslon, S.; Guillou, O.; Daguebonne, C.; Totti, F.; Cador, O.; Guizouarn, T.; Le Guennic, B.; Bernot, K., Magnetic Slow Relaxation in a Metal-Organic Framework Made of Chains of Ferro-magnetically Coupled Single-Molecule Magnets. *Chem. Eur. J.* 2018, 24, 6983-6991.
30. Korzyński, M. D.; Berkson, Z. J.; Le Guennic, B.; Cador, O.; Copéret, C., Leveraging Surface Siloxide Electronics to Enhance the Relaxation Properties of a Single-Molecule Magnet. *J. Am. Chem. Soc.* 2021, 143, 5438-5444.